Nanoscale elasticity of highly anisotropic pyrocarbons

B. Farbos, Jean-Pierre da Costa, G.L. Vignoles, J.-M. Leyssale

To cite this version:

B. Farbos, Jean-Pierre da Costa, G.L. Vignoles, J.-M. Leyssale. Nanoscale elasticity of highly anisotropic pyrocarbons. Carbon, 2015, 94, pp.285 - 294. 10.1016/j.carbon.2015.06.060 . hal-01717025

HAL Id: hal-01717025
https://hal.science/hal-01717025
Submitted on 9 Sep 2023

Nanoscale elasticity of highly anisotropic pyrocarbons

B. Farbos[a,b,c], J.-P. Da Costa[b], G. L. Vignoles[c], J.-M. Leyssale[a,d,*]

[a] *CNRS, Laboratoire des Composites ThermoStructuraux, UMR 5801*
CNRS-Herakles-CEA-Université de Bordeaux,33600 Pessac, France
[b] *Univ. Bordeaux, BSA, Laboratoire de l'Intégration du Matériau au Système, UMR 5218*
CNRS-IPB - Université de Bordeaux, 33405 Talence, France
[c] *Univ. Bordeaux, Laboratoire des Composites ThermoStructuraux, UMR 5801*
CNRS-Herakles-CEA-Université de Bordeaux, 33600 Pessac, France
[d] *MultiScale Material Science for Energy and Environment, CNRS-MIT, Massachusetts*
Institute of Technology, 77 Massachusetts Avenue, Cambridge, MA 02139

Abstract

We report on the elastic properties of high-textured laminar pyrocarbons (PyCs) as obtained at the nanoscale using atomistic simulations on realistic models of the rough laminar (RL) PyC, the regenerative laminar (ReL) PyC, and the ReL PyC heat treated at temperatures up to 1700°C. The purely longitudinal (C_{11}, C_{12}, C_{66}, E_1 and ν_{12}) and transverse (C_{33} and E_3) elastic properties of such materials have values of around 50-75 % of those found for graphite. Conversely, cross longitudinal-transverse properties (C_{13}, C_{44}, ν_{13} and ν_{31}) are much larger in PyCs than in graphite (up to around one order of magnitude for ν_{31}). Our results also show that stiffness decreases with the hydrogen content, that longitudinal properties increase with the extent of graphene domains and decrease with the misorientation of the layers, and that transverse and cross properties significantly increase with the amount of

---

[*] Corresponding author
Email address: `leyssale@lcts.u-bordeaux1.fr, leyssale@mit.ed` (J.-M. Leyssale)

Preprint submitted to Carbon *May 28, 2015*

interlayer cross-links present in the materials. Comparison to known experimental data indicates that texture effect at superior scales play an important role in the effective macroscopic elasticity constants. Finally, from a materials perspective and in agreement with the structural evolution, the elastic properties of the ReL PyC evolve with heat treatment towards those of the RL PyC.

1. Introduction

Carbon/Carbon (C/C) composite materials have been known for a very long time for their exceptional mechanical and thermal properties. Their ability to keep a high degree of rigidity up to temperatures of more than 3000 °C in an inert atmosphere makes them extremely valuable as structural parts for applications requiring high mechanical loads under extremely severe temperature conditions. This is the case for many devices used in the aerospace area, like rocket boosters or heat-shield parts for atmospheric re-entry for instance. C/C composites are usually obtained through the deposition of a carbon matrix on a carbon fiber cloth, using different possible chemical routes, from gas or liquid precursors. Understanding the mechanical and thermal behavior of such composite materials is not straightforward and usually requires multiscale models in which the materials scale is described using finite element methods considering effective properties for the fibers and matrix as well as mean field theories [1–4]. Properties of the fibers, both mechanical and thermal, are extremely well documented in the litterature due to the possibility of directly performing the measurements on single filaments. For instance, in the case of ex-pitch high-modulus fibers, these properties have recently been reviewed by Emmerich [5]. Data regarding the properties of matrices, especially those obtained by chemical vapor deposition or infiltration (CVD/I), usually called pyrolytic carbons or pyrocarbons (PyC), are scarce, due to the difficulty of obtaining the latter in bulk form.

Nevertheless, a few studies report on the elastic properties of such PyCs as obtained by acoustic methods [6, 7], micro and nano indentation [8, 9] or uniaxial tension/compression tests [10, 11]. High textured PyCs are isotropically transverse materials with a supposed high anisotropy of properties. ~~:~~ ~~for instance the elastic constants of graphite from which they derive~~ It is useful to compare the elastic constants of PyCs with those of graphite, which vary from ≈ 1 TPa in the basal direction (C_{11}) to ≈ 25 GPa in the transverse c direction (C_{33}). Experimental estimations of the transverse Young modulus obtained for high-textured PyCs are usually rather close to graphite's C_{33} [6–9]. This is however usually not the case of in-plane properties. Indeed, C_{11} constants obtained using acoustic methods are in the range 40-50 GPa [6, 7]; indentation moduli are around 10-30 GPa, *i.e.* lower or equal to the transverse values [8, 12]; longitudinal moduli from tensile/compression tests show values ranging from around 20 GPa [11] to 200 GPa for as-prepared PyCs [10] and up to 400 GPa when heat treated at high temperature (2200°C)[10].

Atomistic simulations have emerged in the past years as particularly convenient techniques to study the properties of materials down to the nanometer scale. Especially, they have allowed elucidating in great details the structure-property relationship of complex carbon systems such as carbon fibers [13] and polycristalline graphenes [14–16]. In recent work we have presented realistic atomistic models of the rough laminar (RL) and regenerative laminar (ReL) PyCs - including materials heat-treated up to 1700°C - able to describe their nanotexture and nanostructure with great accuracy [17]. In this work we present a detailed investigation of the elastic properties of these highly anisotropic, or high-textured, PyCs and their relationships with nano-structural/-textural parameters.

2. Materials

Nine PyC models, described in details in Ref. 17, are investigated in this work. These models have been obtained using ~~data inferred from HRTEM images and atomistic simulated annealing using~~ the image guided atomistic reconstruction (IGAR) method [18, 19]. The IGAR method is essentially a liquid quench molecular dynamics (LQMD) simulation: a liquid sample (at the composition and density of the corresponding material) is cooled as slowly as possible using a reactive empirical force field. The difference with LQMD is that in IGAR the atoms also feel an external potential based on information collected on actual HRTEM im[illegible]. More specifically, this potential field is directly proportional to the grey levels of a 3D HRTEM image synthesized [illegible]ollow some statistical descriptors derived from the experimental, 2D, HRTEM image. In this way the atoms are slowly driven during the quench toward the dark areas of the 3D HRTEM image. After the quench, the external potential is removed and the system is simulated at constant pressure to relax every possible diagonal internal stress elements.

The accuracy of the models considered in this work has been checked with respect to neutron and X-ray diffraction data [17]. They correspond to roughly cubic systems of ≈ 6.2 nm edge length of five different materials: a rough laminar (RL) PyC, a regenerative laminar (ReL) PyC, and a ReL PyC heat treated at 1300°C (ReL_{1300}), 1500°C (ReL_{1500}) and 1700°C (ReL_{1700}). In addition, hydrogen-free models of similar sizes of the RL and ReL PyC, noted respectively RL(*) and ReL(*), are also considered as well as two larger models (of $\approx$ 12.4 nm edge length) of the RL and ReL PyCs. The latter are noted RL(L) and ReL(L) in what follows. Finally a roughly cubic system of hexagonal graphite (of $\approx$ 6.2 nm edge length) is also considered for comparison. By convention, x and y axes will refer in what follows to in-plane directions and the z axis to the out-of-plane (stacking) direction. In graphite x and y will correspond to armchair (AC) and zigzag (ZZ) directions.

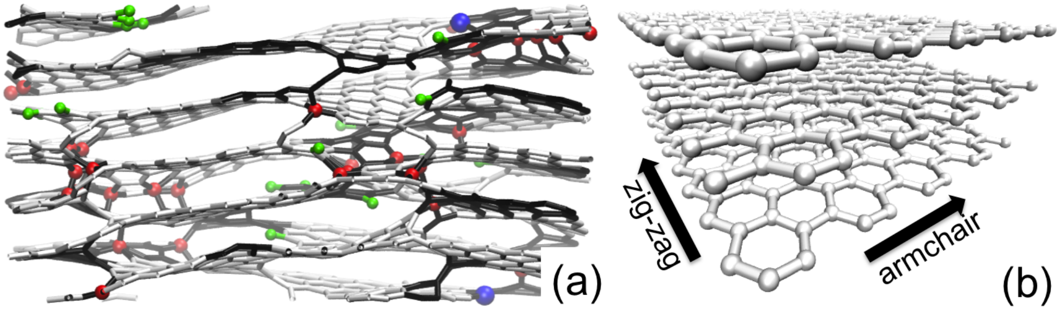

Figure 1: Ball and stick representations of the RL(L) pyrocarbon (a) and hexagonal graphite (b) models used in this work to predict elastic properties. White: purely hexagonal environments; black: defects; green, blue and red spheres in (a) represent hydrogen, twofold carbon and fourfold carbon atoms respectively; arrows in (b) indicate the armchair (AC) and zigzag (ZZ) directions in graphite.

The structure of a PyC model (RL(L)) is compared to the one of graphite in Fig. 1. As can be seen, PyCs are made of nanosized graphene domains connected together by grain boundaries (made of pentagon/heptagon pairs) and interlayer cross-links. The latter participate to a network of screw dislocations through the material and can contain substantial amounts of sp^3 hybridized carbon atoms in addition to curved networks of sp^2 rings. Very localized graphene edges, hydrogenated or unsaturated, can also be found. Some data, characterizing these different models and their experimental counterparts, are summarized in Table 1. A more thorough description can be found in Ref. 17.

As shown in table 1 the models rather accurately reproduce most of the structural and textural features of their experimental counterparts. This is the case for the density, in-plane coherence length L_a from XRD, the average fringe length L_2 and the misorientation angle β_{MOD} from HRTEM analysis and the sp^3 content from NMR. However, out-of-plane properties from XRD, L_c and d_{002}, are respectively significantly under and overestimated in the models, certainly partly due to the used interatomic potential (see the discussion in Ref. 17). Nevertheless, analysis of all these properties reveals a significant increase in structural and textural coherence during the heat treatment process of the ReL PyC. From both points of view of structure and texture, RL PyC is closest to ReL$_{1500}$. Finally it is worth recalling that the ReL$_{1700}$ PyC model, because of its small size ($\approx L_a$ or $L_c/2$), looks more disordered than the prevailing experimental material. A slight underestimation of the structural properties was also observed in the pair distribution function ($r^2G(r)$) analysis of the ReL$_{1300}$ PyC model [17].

3. Methods

Elastic properties of the different model materials were obtained from a few different simulation approaches. In all these calculations periodic bound-

Table 1: Composition and structural data of the pyrocarbon models. d: density; H: hydrogen content; L_a (resp. L_c): in-plane (resp. out-of-plane) coherence length from X-ray diffraction, d_{002}: interlayer spacing from X-ray diffraction; L_2 and β_{MOD}: respectively the average fringe length and grain misorientation from HRTEM analysis [20]; sp^3: fraction of fourfold atoms; f_{hex}: fraction of purely hexagonal atoms (defined as the product of the fraction of threefold atoms by the fraction of atoms belonging to purely hexagonal rings (pC_6^r in Refs 17, 19) among threefold atoms (pC_6^r rings are defined as hexagonal rings made by threefold atoms belonging only to hexagonal rings)). Available experimental data from He pycnometry, elastic recoil detection analysis - secondary ion mass spectroscopy, X-ray diffraction and HRTEM analysis [17, 21] as well as ^{13}C MAS NMR [22] are given for comparison.

Model	d(g/cm^3)		H (at. %)		L_a (nm)		L_c (nm)		d_{002}(nm)		L_2(nm)		β_{MOD}(°)		sp^3(%)	f_{hex}(%)
	Sim.	Exp.	Sim.	Exp.	Sim.	Exp.	Sim.	Exp.	Sim.	Exp.	Sim.	Exp.	Sim.	Exp.	Sim.	Sim.
RL(L)	2.12		0.7		4.9		1.8		0.351		1.6		8.6		1.7	75.8
RL	2.13	2.12	0.7	0.7	4.4	4.6	2.0	5.2	0.355	0.345	1.5	1.1	8.9	8.5	1.7	75.0
RL(*)	2.15		0		4.1		2.2		0.356		1.4		9.2		1.9	74.1
ReL(L)	2.07		2.4		3.3		1.6		0.360		1.0		11.1		2.0	69.5
ReL	2.05	2.11	2.5	2.5	3.3	2.6	1.7	2.9	0.366	0.346	1.0	1.0	11.0	10.1	1.9[a]	66.8
ReL(*)	2.16		0		3.8		1.7		0.354		1.0		9.4		3.1	69.6
ReL$_{1300}$	2.15	2.16	0	0	3.7	3.1	1.8	3.8	0.353	0.347	1.0	1.0	11.0	10.2	2.8	67.0
ReL$_{1500}$	2.17	2.18	0	0	4.7	4.1	2.3	6.3	0.353	0.345	1.4	1.4	8.1	8.3	2.3	74.2
ReL$_{1700}$	2.16	2.18	0	0	4.7	6.2	2.5	13.3	0.353	0.343	1.5	1.9	8.5	7.1	2.0	76.4

---

[a] Compare to ≈ 1.5 % according to ^{13}C MAS NMR experiments[22].

ary conditions were applied in the three dimensions of space. Interactions between carbon (and hydrogen) atoms were accounted for by the second generation reactive empirical bond order potential (REBO) [23], complemented by van der Waals interactions introduced in an adaptative fashion[24]. Elastic constants $C_{\alpha\beta}$ (with $\alpha, \beta = 1, 3$) were obtained from constrained uniaxial tensile (CUATT) and compressive (CUACT) tests using constant temperature molecular dynamics (MD) simulations. In these simulations, a tensile/compressive strain was applied at every step in one direction (α) by a small homothetic deformation of the simulation cell in this direction, the remaining two dimensions being kept fixed. Similarly, constants C_{44} and C_{66} were obtained from uniaxial shear tests (UAST) using constant temperature MD in which a uniform shear strain increment is applied at every step through the use of Lees-Edwards (LE) boundary conditions [25]. The rotation component (one half) of the shear strain under LE deformation was subtracted prior to analysis. An engineering strain rate of 1 ns^{-1} was used in most calculations. A five times larger rate was used for calculations on the large systems requiring access to large strain levels (CUATT) of up to 3 %. The temperature was fixed to 300K using an Andersen thermostat [26] operating with a collision frequency of 1 ps^{-1}. Equations of motion are integrated with the velocity-Verlet algorithm [27] using time steps of 0.5 and 0.25 fs for hydrogen-free and hydrogen-containing systems, respectively.

Finally, Young's moduli (E_α, $\alpha = 1, 3$) and Poisson coefficients ($\nu_{\alpha\beta}$, $\alpha, \beta = 1, 3$) were computed from unconstrained uniaxial tensile (UUATT) and compressive (UUACT) tests using a hybrid Monte Carlo (HMC) technique [28, 29]. In these simulations short constant energy molecular dynamics trajectories as well as Monte Carlo volume changes (in one of the two orthogonal directions to the tension or compression direction) are attempted and either accepted or rejected according to a Metropolis acceptance criterion (depending on volume and temperature for MD attempts, on volume, temperature and stress component for volume change attempts). As for the constrained case, a constant engineering strain increment is applied to the system after every HMC step (either accepted or rejected). This results in simulating a system in which a strain is applied to one direction and the cell length in the two other directions constantly relax to cancel the corresponding diagonal stress components. As HMC is essentially a Monte Carlo sampling technique the strain rate is not as simply defined as in a MD simulation. However, from the average length of the MD trajectories and their acceptance and attempt rates, one can estimate that it is close to the one used in MD (1 ns^{-1}).

Elastic constants C_{11}, C_{33}, C_{12} and C_{13} are obtained from constrained tensile or compressive simulations (CUATT or CUACT). C_{44} and C_{66} are extracted from shear simulations (UAST), Young's moduli (E_1 and E_3) and Poisson coefficients (ν_{12}, ν_{13} and ν_{31}) from unconstrained UUATT or UUACT simulations. Data obtained from tensile, compressive or shear simulations are indicated with T, C and S superscripts, respectively. Engineering strains are converted to true strains before analysis of the strain-stress curves. A more detailed description of the derivation of these data from simulation results is provided in the supporting information.

In former work some inaccuracies, including non-linear elastic effects at low strains, were identified regarding the calculations of the elastic constants of graphene with the REBO potential [30]. These issues, discussed in more details in the supporting information, are recovered here in the case of graphite and PyCs. For instance we have noticed that tensile tests may exhibit two linear regimes depending on the considered strain range: one at low strains, up to 1 (CUATT) or 2 % (UUATT) strain for PyCs, and the second one typically in the [0.01:0.03] and [0.02:0.05] strain ranges for CUATT and UUATT resepectively. As a result, the elastic properties presented in what follows are not fully quantitative and should be considered as only valid in the specified strain domains. For the very same reason, elasticity relationships between the different constants do not strictly hold here, especially when the constants are not obtained in the same strain range. Longitudinal compressive tests reveal a very limited elastic domain, up to 0.01 for PyCs and 0.003 for graphite. Shear simulations show a rather extended and unique linear domain, simplifying the determination of C_{66} and C_{44}. More details regarding the extraction of elastic constants from simulation data are given in the supporting information.

4. Results

4.1. Elastic properties of graphite

Before discussing the elastic properties of PyC models we briefly describe the properties of graphite, as obtained with the REBO potential. The elastic constants of graphite obtained from CUATT ($C^T_{\alpha\beta}$), CUACT ($C^C_{\alpha\beta}$) and UAST ($C^S_{\alpha\alpha}$) are given in table 2. The obtained results are rather consistent, with values around 900, 35, 210, 5, 350 and 0.5 GPa for C_{11}, C_{33}, C_{12}, C_{13}, C_{66} and C_{44}, respectively. C_{66} values from UAST calculations are in fair agree-

Table 2: Elastic constants (in GPa) of hexagonal graphite from constrained tensile ($C^T_{\alpha\beta}$), compressive($C^C_{\alpha\beta}$) and shear ($C^S_{\alpha\alpha}$) MD simulations. Data were obtained in the [0:0.01] strain range for tensions along the arm-chair (AC), zigzag (ZZ) and c directions as well as compression along the c direction. AC and ZZ compressive tests were analyzed in the [0:0.003] strain range, shear tests in the [0:0.005] strain range (numbers in parentheses are error bars on the last digit).

Model	C^T_{11}	C^C_{11}	C^T_{33}	C^C_{33}	C^T_{12}	C^C_{12}	C^T_{13}	C^C_{13}	C^S_{66}	C^S_{44}
AC	912	876			203	208	3	6	350	0.6
ZZ	890	913			224	203	3	5	348	0.6
c			31	37.5			8	2		0.3
Exp. [31] [a]	1060(20)		36(1)		180(20)		15(5)		440(20)	0.18(35)
Exp. [32] [b]	1109(16)		39(1)		139(36)		0(3)		485(10)	5.0(3)

---

[a] Ultrasonic, sonic resonance and static tests

[b] Inelastic X-ray scattering

ment with those (ranging from 335 to 355 GPa) one can obtain from tensile and compressive tests using the elasticity relationship $C_{66} = (C_{11} - C_{12})/2$. These results are also in rather good agreement with experimental values [31, 32], although some deviations can be noticed. As in the case of graphene [30], C_{11} is significantly underestimated (of around 200 GPa) by the REBO potential. Conversely, C_{12} is slightly overestimated. As a result, C_{66} is thus underestimated, of 100-140 GPa. C_{33}, C_{13} and C_{44} are within the range of reported experimental values. It is worth noting that the values reported here for C_{11} and C_{12} are slightly higher than those obtained on graphene [30]. These tiny differences certainly arise from the inclusion of van der Waals interactions (which also act between atoms from the same graphene layer) and from limited out-of-plane mobility in graphite with respect to graphene. These two effects tend toward increasing in-plane stiffness.

Young's moduli and Poisson coefficients computed from UUATT and UUACT HMC simulations are given in table 3. As for C_{11}, the longitudinal Young's modulus E_1 is significantly underestimated by the REBO potential. The values, in close agreement with those obtained for graphene [30], range from 835 (tension along the ZZ direction) to 899 GPa (compression along the ZZ direction), with significant chirality effects. As for graphene as well[30], strong non linearity effects are obtained for tests performed along the ZZ direction with E_1 droping from 835 GPa in the [0:0.01] strain range to 785 GPa in [0:0.03]. The transverse modulus E_3 is close to the experimental value (36 GPa). The Poisson's ratio ν_{12} (0.24) is ≈ 50 % larger than the experimental value whereas ν_{13} (0.10) and ν_{31} (0.004) are approximetely three times lower [31].

Table 3: Young's moduli (in GPa) and Poisson coefficients of hexagonal graphite from unconstrained tensile (indicated by a T superscript) and compressive (C superscript) HMC simulations. All the data but ν_{31} were obtained in the [0:0.01] strain range, ν_{31} being very small, was obtained in the larger [0:0.04] range (numbers in parentheses are error bars on the last digit, one standard deviation on data obtained from independent simulations in the present work).

Model	E_1^T	E_1^C	E_3^T	E_3^C	ν_{12}^T	ν_{12}^C	ν_{13}^T	ν_{13}^C	ν_{31}^T	ν_{31}^C
AC	875	854			0.22	0.27	0.09	0.10		
ZZ	835[a]	899			0.26	0.22	0.08	0.11		
c			32	37					0.004(1)	0.004(1)
Exp. [31] [b]	1020(30)		36(1)		0.16(3)		0.34(8)		0.012(3)	

---

[a] E_1^T falls down to 785 GPa when considering the [0:0.03] strain range; the other moduli do not vary by more than 4 GPa.

[b] Ultrasonic, sonic resonance and static tests.

4.2. Elastic properties of pyrocarbon models

The elastic constants obtained from CUATT, CUACT and UAST MD simulations for the different PyC models are given in table 4. Interestingly, the obtained in-plane stiffnesses are extremely high with C_{11}^T ranging from 525 for PyC ReL to 661 for PyC ReL$_{1700}$ as computed in the largest linear domain (from 0.01 to 0.03 strain) of the stress-strain curves. These values correspond to respectively 58 and 73 % of the value obtained for graphite, 901 GPa by taking the average of AC and ZZ directions. Data from compression tests (C_{11}^C), obtained in the [0:0.01] strain range, are 60-120 GPa lower than those obtained in tension (note that the difference drops to 35-80 GPa when considering C_{11}^T values obtained in the [0:0.01] strain range as reported in the supporting information). In-plane Young's moduli (table 5) are consistent with these data with values of E_1^T and E_1^C ranging from 538 (ReL) to 658 (ReL$_{1700}$) GPa and from 416 (ReLH) to 569 (ReL$_{1700}$) GPa, respectively.

The other in-plane properties include the off-diagonal elastic constant C_{12}, Poisson's ratio ν_{12} and in-plane shear elastic constant C_{66}. Tensile C_{12}^T ranges from 96 (ReL) to 123 GPa (RL), which accounts for ≈ 50 % of graphite's C_{12} (210 GPa). Compressive C_{12}^C are close to C_{12}^T values. Tensile and compressive ν_{12} are found around 0.17 ± 0.02 and 0.13 ± 0.02, respectively, which is lower than the average value of 0.24 obtained for graphite. All PyC models show C_{66} values between 225 and 244 GPa (*i. e.* 2/3 of the value for graphite) except ReL PyC, at 190 GPa.

The two purely transverse elastic properties are C_{33} and E_3. Tensile and compressive C_{33} (table 4) range from 20 to 27 GPa and from 25 to 35 GPa respectively with lowest values obtained for the RL(*) model and largest for

Table 4: Elastic constants (in GPa) of pyrocarbon models obtained from constrained tensile ($C^T_{\alpha\beta}$), compressive($C^C_{\alpha\beta}$) and shear ($C^S_{\alpha\alpha}$) MD simulations (considered true strain ranges were of [0.01:0.03], [0:0.005] and [0:0.01] for tensile, compressive and shear tests, respectively; numbers in parentheses are the standard deviations on the last digit obtained from independent simulations (tensile tests in x and y for C^T_{11} for instance); proportions (in %) with respect to the corresponding values for graphite (table 2) are given in square brackets bleow the absolute values).

Model	C^T_{11}[a]	C^T_{33}[b]	C^T_{12}[c]	C^T_{13}[d]	C^C_{11}	C^C_{33}	C^C_{12}	C^C_{13}	C^S_{66}	C^S_{44}
RL(L)	624(2)	20	115(1)	22(4)	521(4)	26	96(1)	26(4)	227(1)	9.3(7)
	[69]	[65]	[54]	[471]	[58]	[69]	[47]	[600]	[65]	[1860]
RL	632(3)	21	123(2)	23(4)	533(12)	28	116(3)	29(1)	235(1)	9.4(7)
	[70]	[68]	[58]	[493]	[60]	[75]	[56]	[669]	[67]	[1880]
RL(*)	641(2)	20	115(3)	24(5)	537(25)	25	109(1)	34(3)	239(1)	9.3(3)
	[71]	[65]	[54]	[514]	[60]	[67]	[53]	[785]	[68]	[1860]
ReL(L)	535(1)	22	102(1)	28(3)	474(5)	27	97(3)	32(3)	194(1)	13.6(6)
	[59]	[71]	[48]	[600]	[53]	[72]	[47]	[738]	[56]	[2720]
ReL	525(1)	21	96(1)	27(2)	453(10)	28	91(2)	33(2)	190(1)	13.4(9)
	[58]	[68]	[45]	[579]	[51]	[75]	[44]	[762]	[54]	[2680]
ReL(*)	608(4)	26	117(1)	31(3)	544(5)	35	116(4)	39(4)	232(1)	14.8(2)
	[67]	[84]	[55]	[664]	[61]	[93]	[56]	[900]	[66]	[2960]
ReL$_{1300}$	593(2)	27	114(1)	30(3)	521(16)	32	109(3)	36(5)	225(1)	15.4(4)
	[66]	[87]	[53]	[643]	[58]	[85]	[53]	[831]	[64]	[3080]
ReL$_{1500}$	654(3)	23	120(1)	24(4)	553(1)	32	109(8)	31(6)	244(1)	9.5(5)
	[73]	[74]	[56]	[514]	[62]	[85]	[53]	[715]	[70]	[1900]
ReL$_{1700}$	661(4)	21	113(1)	20(4)	539(3)	26	88(3)	23(6)	239(1)	7.2(8)
	[73]	[68]	[53]	[429]	[60]	[69]	[43]	[531]	[68]	[1440]

---

[a] 25-45 GPa lower in the [0:0.01] strain range.

[b] 4-5 GPa larger in the [0:0.01] strain range.

[c] C_{12} in the [0:0.01] strain range are within the error bars.

[d] 4-6 GPa larger in the [0:0.01] strain range.

Table 5: Young's moduli (in GPa) and Poisson coefficients of pyrocarbon models obtained from unconstrained tensile and compressive MD simulations (the considered true strain range was [0:0.01] for all constants but E_1^T ([0.02:0.05]), ν_{12}^T ([0:0.05]) and E_1^C [0:0.005]; numbers in parentheses are the standard deviations on the last digit obtained from independent simulations; proportions (in %) with respect to the corresponding values for graphite (table 3) are given in square brackets bleow the absolute values).

Model	E_1^T	E_3^T	ν_{12}^T	$\nu_{13}^{T\,a}$	ν_{31}^T	E_1^C	E_3^C	ν_{12}^C	ν_{13}^C	ν_{31}^C
RL	631(7)	22	0.19(2)	0.70(6)	0.04(1)	507(1)	28	0.15(1)	1.09(6)	0.04(1)
	[74]	[69]	[79]	[824]	[1000]	[58]	[76]	[61]	[1038]	[1000]
RL(*)	644(1)	22	0.17(2)	0.86(7)	0.05(1)	524(15)	26	0.11(1)	1.22(6)	0.04(1)
	[75]	[69]	[71]	[1012]	[1250]	[60]	[70]	[45]	[1162]	[1000]
ReL	538(1)	20	0.15(1)	0.98(1)	0.06(1)	416(9)	27	0.10(1)	1.29(3)	0.06(1)
	[63]	[63]	[62]	[1153]	[1500]	[47]	[73]	[41]	[1229]	[1500]
ReL(*)	612(3)	29	0.17(1)	0.92(1)	0.05(1)	478(2)	29	0.14(1)	1.05(1)	0.06(1)
	[72]	[91]	[71]	[1082]	[1250]	[55]	[78]	[57]	[1000]	[1500]
ReL_{1300}	599(2)	29	0.16(2)	0.93(2)	0.06(1)	479(20)	30	0.14(1)	1.06(4)	0.06(1)
	[70]	[91]	[67]	[1094]	[1500]	[55]	[81]	[57]	[1010]	[1500]
ReL_{1500}	652(5)	24	0.18(1)	0.69(2)	0.04(1)	535(15)	31	0.14(1)	1.03(1)	0.04(1)
	[76]	[75]	[75]	[812]	[1000]	[61]	[84]	[57]	[981]	[1000]
ReL_{1700}	658(1)	24	0.17(1)	0.76(1)	0.04(2)	569(13)	28	0.11(2)	0.99(1)	0.04(1)
	[77]	[75]	[71]	[894]	[1000]	[65]	[76]	[45]	[943]	[1000]

---

[a] $\approx$ 0.4 lower values are obtained in the extended [0.02:0.05] second linear domain.

the ReL(*) or ReL$_{1300}$ models. These values are $\approx$ 30 % lower than those obtained for graphite. As for graphite, E_3^T and E_3^C (table 5) are usually very close to C_{33}^T and C_{33}^C, respectively.

The remaining elastic constants, C_{13}, C_{44}, ν_{13} and ν_{31}, couple longitudinal and transverse properties. C_{13}^T obtained from constrained tensile simulations ranges from 20 (ReL$_{1700}$) to 31 (ReL(*)) GPa (values obtained in the [0:0.01] strain range, 4-6 GPa larger, are almost identical to C_{13}^C values). These values are significantly larger ($\approx$ by a factor 5) than those obtained for graphite (see table 2). C_{44} ranges from 7.2 GPa for PyC ReL$_{1700}$ to 15.4 GPa for PyC ReL$_{1300}$: it is around 15 to 30 times larger than for graphite. ν_{13}, characterizing the transverse response of the unit cell to a longitudinal strain, ranges from 0.7 (RL and ReL$_{1500}$) to 1 (ReL) for tensile simulations and from 1 (ReL$_{1700}$) to 1.3 (ReL) for compressive simulations. ν_{31}, characterizing the longitudinal response to a transverse strain, is around 0.05 for all PyC models and from both tensile and compressive unconstrained simulations. These Poisson coefficients are around one order of magnitude larger than for graphite.

Before discussing the structure-property relationships in these materials we briefly discuss on the relationships existing between the different elastic properties presented in tables 4 and 5. Especially, for a transverse isotropic material, linear elasticity predicts that the following relationships should hold:

$$\frac{E_1}{C_{11} - \nu_{12} C_{12}} = 1 \tag{1}$$

$$\frac{2C_{66}}{C_{11} - C_{12}} = 1 \tag{2}$$

$$\frac{\nu_{13}E_3}{E_1\nu_{31}} = 1. \tag{3}$$

The ratios at the left hand sides of Eqs. 1, 2 and 3 have been computed using all the data sets provided in tables 4 and 5. Values in the ranges [1.02:1.06] and [1.1:1.2] were obtained for Eq. 1 with tensile and compressive elastic constants, respectively. For Eq. 2 we obtained ratios of [0.87:0.95] (tensile + shear) and [0.92:1.12] (compressive + shear) and ratios of [1.1:1.7] (tensile) and [0.5:0.95] (compressive) were obtained for Eq. 3. As can be seen Eqs 1 and 2 are relatively well satisified by our data, although some deviations are observed because of ~~some~~ non-linearity effects arising from the used interatomic potential. These deviations from linearity, thoroughly discussed in Ref. 30 in the case of graphene and in the supporting information for PyCs, are responsible for the different strain domains used in the present work to fit different eleastic constants. Data obtained for the ratio of Eq. 3 show significantly larger deviations to unity. This is both due to the interatomic potential and to large error bars on some computed elastic constants (up to 25 % for ν_{31}).

Another interesting point from these results is that the elastic constants obtained for the RL(L) and ReL(L) models, twice as long (*i.e.* 8 times larger volumes) as their corresponding smaller RL and ReL models, are within the error bars of those obtained for the latter (see table 4). This is a clear indication that size effects are very limited at these scales and that, in other words, the properties reported in this work are meaningful elastic properties of bulk PyC, down to the nanoscale (apart from the small inaccuracies due to the REBO potential).

Finally, from simulations performed without accounting for van der Waals

Table 6: Elastic constants C_{33}^{T*}, C_{13}^{T*} and C_{44}^{S*} obtained from simulations not incorporating van der Waals interactions (numbers in parentheses are the standard deviations on the last digit obtained from independent simulations).

Model	C_{33}^{T*}	C_{13}^{T*}	C_{44}^{S*}
RL	3.3	13.6(16)	6.7(5)
RL(*)	3.4	10.8(4)	7.3(5)
ReL	5.0	13.9(7)	10.8(8)
ReL(*)	6.3	16.9(1)	12.1(4)
ReL_{1300}	6.0	16.3(12)	12.5(8)
ReL_{1500}	4.0	13.1(3)	7.0(5)
ReL_{1700}	2.7	8.0(13)	5.9(7)

interactions we can determine the contribution of covalent bonding to the elastic properties (note this is only an approximation as, due to relaxation, the systems adopt slightly different densities). In-plane properties, essentially due to covalent bonding, are almost unaffected by the presence or not of van der Waals interactions and will not be discussed here. Tensile C_{33}^{T*}, C_{13}^{T*} and shear C_{44}^{S*} constants obtained without van der Waals inteactions are given in table 6. As can be seen, C_{33}^{T*} ranges from 2.7 to 6.3 GPa. This accounts for 13 % (ReL_{1700}) to 25 % (ReL(*)) of the total C_{33}^{T}. The effect of covalent bonding is much higher for C_{13} and C_{44}, with contributions around 50 and 70 %, respectively. Note that, taking into account the very low C_{44} obtained for graphite (≈ 0.5 GPa), we would expect a covalent contribution to C_{44} in pyrocarbons close to 100 %. This is actually certainly the case; the larger values of C_{44}^{S} with respect to C_{44}^{S*} are probably essentially due to structural relaxation in the latter rather than to van der Waals interactions.

4.3. Structure/property relationship

Summarizing the results of the former section we have seen that in-plane stiffness (C_{11}, C_{12}, C_{66}, E_1 and ν_{12}) increases when going from the raw ReL PyC to the heat treated samples at the highest temperatures (1500 and 1700°C), which seems consistent with an increase of the "graphene" content, as visually inferred from the models (see Ref. 17) or characterized using indicators like L_a or the amount of "hexagonal" atoms: f_{hex}. Conversely, transverse properties (C_{33} and E_3) and cross properties (C_{13}, C_{44}, ν_{13} and ν_{31}) decrease with heat treatments, which seems to correlate with a decrease of the amount of interlayer cross-links observed in the models. Also, in fair agreement with structural and textural considerations (see table 1) we have observed that the RL PyC's elastic properties are close to those of ReL$_{1500}$. Finally, the data reported in tables 4 and 5 also indicate that the presence of hydrogen significantly decreases the mechanical properties. For instance, elastic constants obtained for the fully carbonaceous ReL(*) model are ≈ 20 % larger (see table 4) than those obtained for the ReL PyC model, containing 2.5 at. % of hydrogen. Hydrogen being essentially found at graphene edges, we easily understand that when it is not incorporated into the models, some of these edges are replaced by covalent bonds between adjacent graphene domains in-plane (grain boundaries) and out-of-plane cross-links, thus increasing stiffness.

In what follows we attempt to derive some relationships beween the nanostructure of these pyrocarbons and the elastic properties at the nanoscale derived from atomistic simulations. Longitudinal properties, expected to correlate with the lateral extension of graphene layers, are compared to the in-plane coherence length L_a and to the fraction of purely hexagonal atoms (f_{hex}). Transverse and cross properties, expected to depend on the coherence of layer stacking and on the network of interlayer cross-links, are compared to L_c and to the fraction of sp^3 atoms. The latter descriptor, although not being a direct measurement of the amount of interlayer cross-links, is certainly a good indicator of their presence as can be seen in Fig. 1(a).

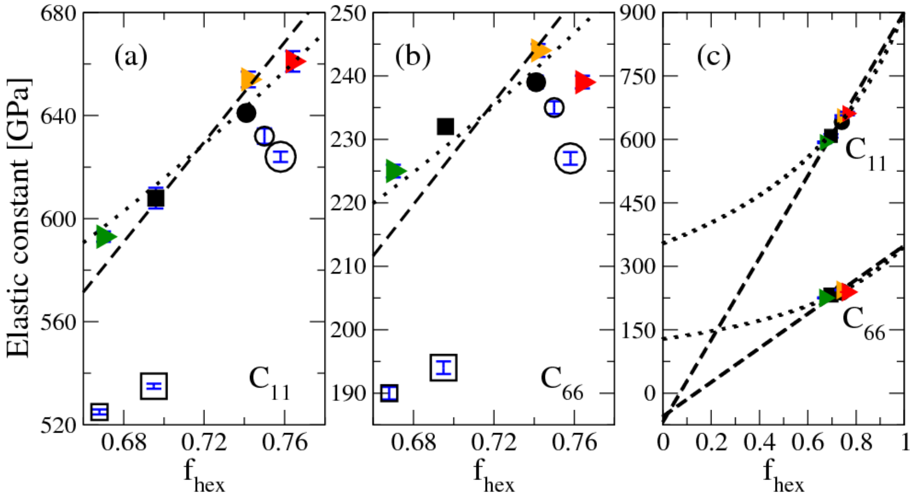

Figure 2: Evolution of C_{11}^T (a) and C_{66}^S (b) with the fraction of purely hexagonal atoms f_{hex}. Circles: RL; squares: ReL; triangles: ReL heat treated at 1300 (green), 1500 (orange) and 1700 (red) °C; empty symbols: hydrogenated PyCs; lines: fits of Eq. 4 (dashed) and Eq. 5 (dotted), considering $f_{hex} = \phi_G$, on non hydrogenated PyCs (panel (c) displays all the data of the fully carbonaceous models in the extended [0:1] f_{hex} range, for a visualization purpose).

Evolutions with f_{hex} of C_{11} and C_{66}, obtained from tensile and shear MD simulations, are given in Fig. 2. E_1, showing a very similar behavior to the one of C_{11}, as well as C_{12}, for which no trend can be observed due to extremely close values between the different models, are not discussed here. In both cases, a clear increase of the elastic constant with f_{hex} is observed for the fully carbonaceous models (as mentioned earlier, hydrogen containing models (RL and ReL) have lower stiffness than their fully carbonaceous counterparts).

The data of Fig. 2 can be interpreted using a simple 2D model consisting of circular graphene disks (of radius $L_a/2$) connected together by grain boundaries (of thickness l).

The two following mechanical models, where C_{ii}^G and C_{ii}^{GB} are the elastic constants of graphite (G) and grain boundaries (GB), respectively, can be used to describe the in-plane elastic constants of the system as a function of the graphene fraction ϕ_G:

$$C_{ii} = \phi_G C_{ii}^G + (1 - \phi_G) C_{ii}^{GB} \tag{4}$$

$$C_{ii} = \left(\frac{\phi_G}{C_{ii}^G} + \frac{1 - \phi_G}{C_{ii}^{GB}} \right)^{-1} \tag{5}$$

Eqs. (4) and (5) consider arrangements of graphene and grain boundaries respectively in parallel (Voigt model) and series (Reuss model) with respect to the stress direction. Using graphite's C_{11}^G and C_{66}^G, namely 901 and 349 GPa (see table 2) and assuming that f_{hex} is a reasonable approximation of ϕ_G, Eqs 4 and 5 can be used to determine upper and lower bounds of C_{11}^{GB} and C_{66}^{GB} by fitting the data concerning the five fully carbonaceous models in Figs 2(a,b). Note that, within this framework, Voigt and Reuss models do not correpsond to upper and lower bounds of the composite as they rely on different properties for one of the constituents. The fits, displayed in Fig. 2, although not being perfect, allow the determination of the following values:

C_{11}^{GB} = -68 GPa (Voigt) and 354 GPa (Reuss); C_{66}^{GB} = -55 GPa (Voigt) and 128 GPa (Reuss). Predictions obtained with Voigt's model (negative) are unrealistic; this is expected as this model implies that no GB are crossed along the strain direction. This is highly unrealistic in our virtual materials for which the average dimension of the graphene layers (3 nm $< L_a <$ 5 nm) is significantly smaller than the length of the simulation cells (6.2 or 12.4 nm). Reuss' predictions, however, are pretty reasonable and, for instance, were recently employed for modeling ex-pitch high-modulus carbon fibers [5]. Indeed, considering that GB are heterogeneous mixtures of stiff clusters of pentagons, heptagons and hexagons, resembling the haeckelite graphene allotrope [33] for which our calculations indicate a value of $\approx$ 750 GPa for C_{11}, and of weak graphene edges and interlayer cross-links, a value of 350 GPa as the stiffness of GB ~~is~~ can be quite realistic.

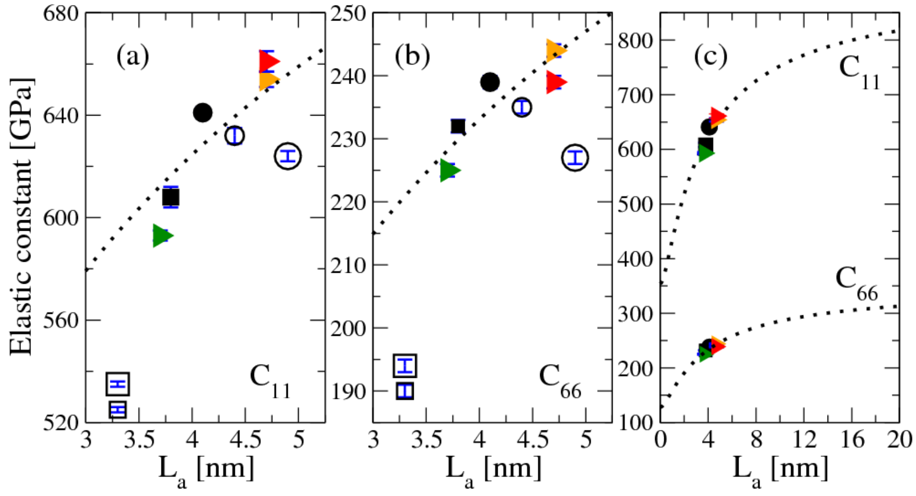

Figure 3: Same as Fig. 2 for the evolutions of C_{11}^{T} (a) and C_{66}^{S} (b) with L_a.

In Figure 3 are plotted the evolutions of C_{11} and C_{66} with L_a. As was observed with f_{hex}, longitudinal stiffness also globally increases with L_a. Coming back to the simple model described previously and considering that a GB is shared by two graphene grains one can easily relate the graphene fraction ϕ_G to L_a and the GB thickness l:

$$\phi_G = \frac{{L_a}^2}{{L_a}^2 + 2L_a l + 2l^2}. \tag{6}$$

Fitting the evolution of f_{hex} with L_a using Eq. 6 we obtain a realistic GB thickness $l = 0.69$ nm. Finally, combining Eqs 5 and 6 we get the evolutions of C_{11} and C_{66} with L_a according to Reuss' model (dotted lines in Fig. 3).

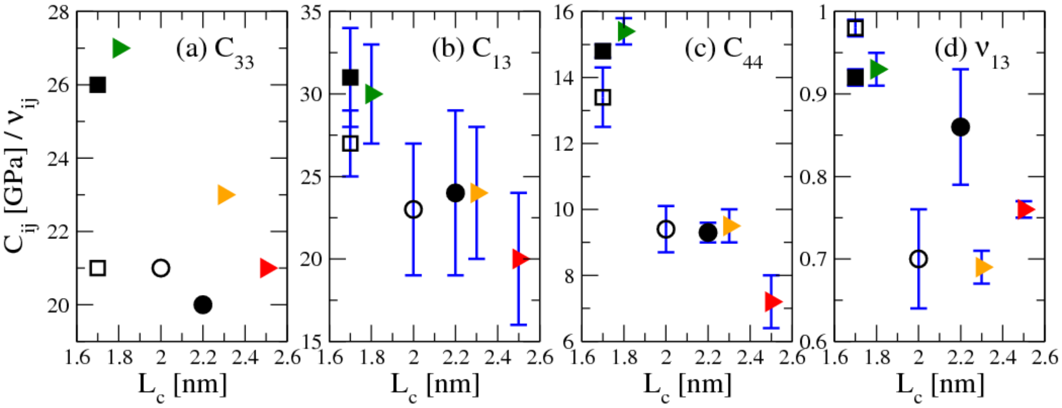

Figure 4: Evolution of C_{33} (a), C_{13} (b), C_{44} (c) and ν_{13} (d) with L_c (same symbol and color codes as in Fig. 2.

Evolutions of transverse (C_{33}) and cross (C_{13}, ν_{13} and C_{44}) properties with the transverse coherence length L_c are shown in Fig. 4. All these properties show a decreasing trend with increasing stacking order. This behavior is somehow expected for C_{13}, ν_{13} and C_{44} as increasing L_c drives the system closer to graphite for which the corresponding constants are lower. The behavior of C_{33} is more unusual as graphite has a higher value (31 GPa). We would thus expect C_{33} to progress (increase) towards graphite's value while increasing L_c. The covalent bonding and van der Waals contributions to C_{33} are plotted against L_c and the fraction of sp^3 atoms in Fig. 5. Bonding contributions were obtained from CUATT neglecting van der Waals interactions, van der Waals ones by subtracting the former to the C_{33} values obtained from tests including van der Waals forces.

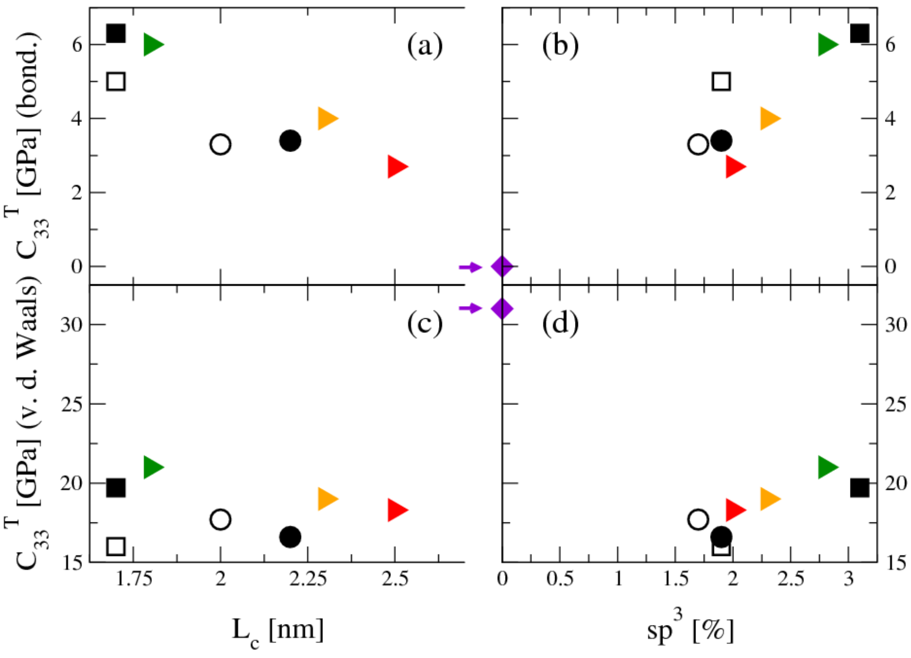

Figure 5: Covalent bonding (a-b) and van der Waals (c-d) contributions to C_{33}^T as a function of L_c (a-c) and the fraction of sp^3 atoms (b-d). (same symbol and color codes as in Fig. 2; graphite's data have been added with purple lozenges and arrows).

Interestingly, we can see that the decrease of C_{33} with increasing L_c is essentially due to the covalent contribution (Fig. 5(a)), which shows a rapid decrease towards zero, the value expected for graphite (infinite L_c). Conversely, the van der Waals contribution (Fig. 5(c)) does not show any specific evolution in the range of L_c values covered by our PyC models (from 1.7 to 2.5 nm). It indeed remains around 18 GPa, pretty far from graphite's value (31 GPa), certainly because of the large overestimation of the interlayer distance d_{002} in our models (see table 1). The increase of the covalent contribution to C_{33} arises from the many interlayer cross-links found in the PyC models. As shown in Fig. 5(b), an almost linear scaling of this term with the fraction of sp^3 atoms can be observed, starting at 0 GPa for graphite, up to ≈ 6 GPa for the ReL(*) and ReL$_{1300}$ models having around 3% of sp^3 atoms.

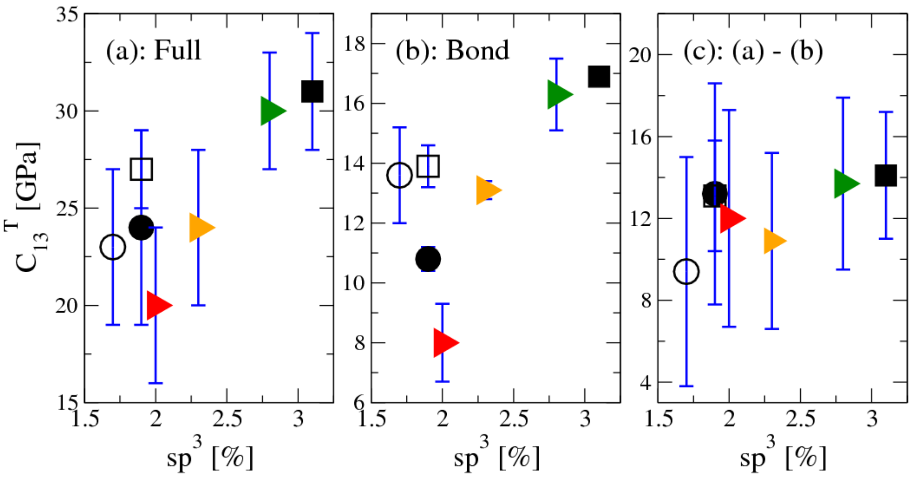

Figure 6: Evolutions of the total C_{13}^T (a), its covalent bonding contribution (b) and the difference between them (c) as a function of the fraction of sp^3 atoms (same symbol and color codes as in Fig. 2).

Full, covalent and van der Waals contributions to C_{13} and C_{44} are displayed against the fraction of sp^3 atoms in Figs 6 and 7, respectively. In both cases, the decrease with L_c observed in Fig. 4 (b,c) can be explained by the

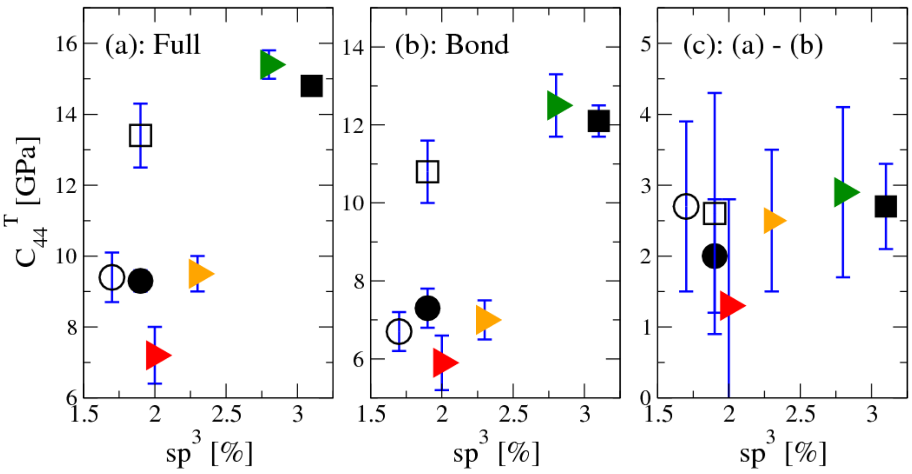

Figure 7: Same as Fig. 6 for C_{44}.

increase of the bonding contributions with the fraction of sp^3 atoms (Figs 6(b) and 7(b)), the van der Waals contributions being almost independent of this structural parameter (Figs 6(c) and 7(c)).

A last textural parameter that we would like to investigate here is the effect of grain orientations. In Figure 8 we show the evolutions of in-plane tensile C_{11} and shear C_{66} constants as a function of the average misorientation angle β_{MOD} between adjacent crystallites, determined from the analysis of simulated HRTEM images [17, 20]. For a better structure-property comparison only hydrogen-free models have been included in the Figure. A very clear decrease of both properties with increasing misorientation is observed. This is in fair agreement with recent theoretical work by Emmerich [5] and Lin *et al.* [3] who have shown that these properties significantly depend on the misorientation of layers. However, it is worth noting that in our data set of materials, β_{MOD} is highly correlated with L_a[17]. It is thus impossi-

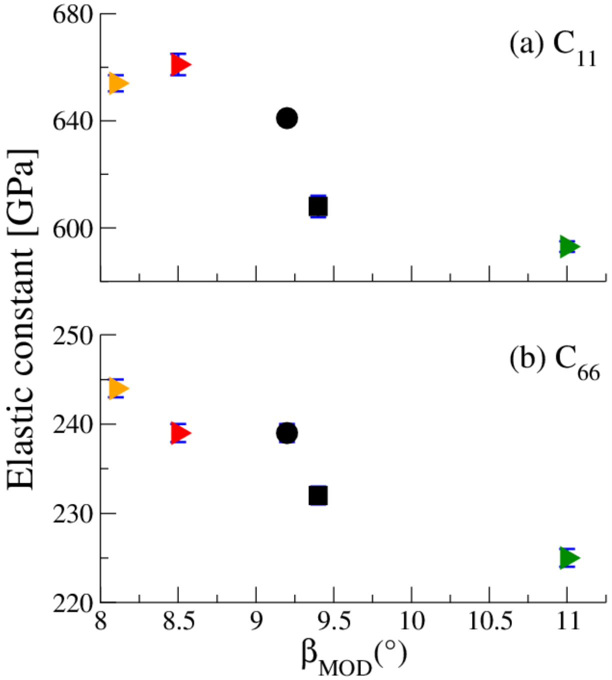

Figure 8: Evolutions of tensile C_{11} (a) and C_{66} (b) with the average intergrain misorientation angle β_{MOD} in hydrogen-free pyrocarbon models (same symbol and color codes as in Fig. 2).

ble to conclude at this point whether the decrease of stiffness observed with increasing β_{MOD} is really an effect of increasing anisotropy or simply connected to the associated decrease of L_a. Obviously this remark also holds for the evolution of stiffness with L_a which may also be affected by a change in anisotropy.

4.4. Comparison to literature data

In table 7 we compare the Young's moduli and Poisson's ratio predicted in this work to experimental data obtained on high textured PyCs. The latter include results from tensile tests performed on low modulus carbon fibers coated by RL and ReL PyCs, as-prepared and after heat treatment at 1600° [10], as well as tensile (TT) and compressive tests (CT) [11], ultrasound phase spectroscopy (US) [7] and three point bending tests (TPB) [9] on a commercial high textured PyC. Existing results from nanoindentation [8, 12, 34, 35] were not included because of serious questions raised in the literature regarding the ability of these methods to separate in-plane and out-of-plane properties [8, 12].

Results on the commercial high textured PyC [7, 9, 11] show extremely low E_1 values, in the range [6:30 GPa]. This is from one to two orders of magnitude lower than our predicitons on RL and ReL PyCs. Values of E_3 obtained for this material [5:13 GPa] are closer to our predictions [20:31 GPa]. Values of ν_{12} and ν_{13} measured in these studied are almost within the range of values obtained in our calculations. However, the experimentally determined ν_{31}, 0.35 and 0.22 according to CT and US experiments, respectively, are 4 to 10 times larger than our nanoscale predictions.

Interestingly, E_1 values from Sauder *et al.* [10] on RL and ReL PyC

Table 7: Experimental Young's moduli (in GPa) and Poisson coefficients of pyrocarbons obtained from tensile (TT), compressive (CT), ultrasonic (US) and three point bending (TPB) tests (our results from HMC simulations are given for comparison).

	Method	E_1	E_3	ν_{12}	ν_{13}	ν_{31}
RL [10]	TT	115(3)				
RL (1600°C)	TT	118(3)				
ReL	TT	205(7)				
ReL (1600°C)	TT	270				
high text. [11]	TT	30(1)		0.16(3)	0.97(4)	
high text.	CT	19(1)	5(1)	0.22(1)		0.35(1)
high text. [7]	US	27	13	0.35	0.47	0.22
high text. [9]	TPB	6-16				
This work	UUATT	538-658	20-29	0.15-0.19	0.69-0.98	0.04-0.06
This work	UUACT	416-569	26-31	0.10-0.15	0.99-1.29	0.04-0.06

matrices are significantly much higher than those obtained on the commercial PyC. They are still lower (by a factor 2 to 6) than the nanoscale values predicted in this work. In this experimental work, the RL PyC has a lower modulus than the ReL PyC, 115 GPa against 205 GPa. In addition, the former does not change much with heat heat treatment while the latter significantly increases. Conversely, according to Sauder *et al.*[10], L_a increases more with heat treatment for the RL PyC than for the ReL PyC. These results suggest that elasticity in macroscopic samples results from a complex interplay between the nano- and microstructure of the material.

Table 8: Effective elastic constants of coherent domains from the micromechanical analysis (MMA) of high textured PyCs by Lin *et al.* [3] (results from the present work are also displayed for comparison).

	Method	C_{11}	C_{33}	C_{12}	C_{13}	C_{66}	C_{44}
Lin *et al.*[3]	MMA	686	90	164	28	261	26
This work	CUATT	525-661	20-27	96-123	20-32		
This work	CUACT	453-539	26-35	91-116	23-39		
This work	UAST					190-244	7-15

Very recently, Lin *et al.* have proposed an interesting micromechanical model of high textured PyC matrices [3]. Based on an orientation analysis of lattice fringe HRTEM images and a homogenization method they were able to derive an effective elastic tensor for the coherent domains at the nanoscale. The obtained elastic constants are given in table 8, together with the range of values obtained in the present work. Interestingly, we can see that almost all constants are within, or close to, the range of values obtained in our simulations. The only striking disagreement between their and our predictions is on C_{33}, for which they obtain a value around three times larger than ours.

5. Conclusions

We have presented a detailed study of the elastic behavior at the nanoscale of several realistic atomistic models of highly anisotropic laminar pyrocarbons. At this scale, purely longitudinal and transverse properties are relatively close (50-75 %) to those of graphite while cross properties are significantly larger. The longitudinal Young's moduli obtained here are much larger than those measured by Sauder *et al.* on the same class of materials [10], indicating that macroscopic properties are not determined only by the bulk structure at the nanoscale. Elements from the microstructure, like misorientation between matrix grains, junction of growth cones, cracks, etc..., certainly plays an important role in the macroscopic behavior of the matrices.

However, our results are extremely consistent with the effective elastic properties of coherent domains obtained at the sub-micro-level in the micromechanical analysis of high textured PyCs by Lin *et al.* [3]. The strength of our work is that these properties were directly determined from the atomic structure of the materials, following a very realistic structure reconstruction. Another advantage of this approach is that it allows investigating the structure/proprety relationship at the nanoscale. Doing this we have been able to show that (i) hydrogen, giving rise to (saturated) graphene edges instead of grain boundaries and interlayer cross-links in fully carbonaceous systems (at constant texture), significantly lowers all elastic constants; (ii) longitudinal properties significantly increase with the extent of graphene layers (as probed by the fraction of hexagonal atoms (f_{hex}) or the simulated in-plane coherence length (L_a)) while they decrease with increasing misorientation (β_{MOD}); and (iii) Transverse and cross properties significantly increase with the amount of cross-links (covalent bonds) between stacked graphene layers.

Acknowledgements

Funding from the Agence Nationale de la Recherche through the PyroMaN project (contract ANR-2010-BLAN-929) and from the Institut Carnot Materials and systems Institute of Bordeaux (MIB) are gratefully acknowledged. Access to the computer facilities of the Mésocentre de Calcul Intensif en Aquitaine (MCIA) is also acknowledged. JML gratefully acknowledges Dr Farhang Radjai for useful discussions on elasticity and the French ICoME2 Labex (Grant ANR-11-LABX-0053) for supporting his stay at MIT.

References

[1] Piat R, Böhlke T, Deutschmann O, Dietrich S, Drach B, Gebert JM, et al. Numerical Studies of the Influence of the Porosity on Macroscopic Elastic Properties of Carbon/Carbon Composites. Proc Appl Math Mech. 2010;10(1):719–720.

[2] Drach B, Tsukrov I, Gross T, Dietrich S, Weidenmann K, Piat R, et al. Numerical modeling of carbon/carbon composites with nanotextured matrix and 3D pores of irregular shapes. Int J Sol Struct. 2011;48(18):2447–2457.

[3] Lin S, Langhoff TA, Böhlke T. Micromechanical estimate of the elastic properties of the coherent domains in pyrolytic carbon. Arch Appl Mech. 2014;84:133–48.

[4] Caty O, Couégnat G, Charron M, Agulhon T, Vignoles GL. Image-Based Numerical Simulation of Thermal Expansion in C/C Composites. Ceram trans. 2014;248:39–44.

[5] Emmerich FG. Youngs modulus, thermal conductivity, electrical resistivity and coefficient of thermal expansion of mesophase pitch-based carbon fibers. Carbon. 2014;79:274 – 93.

[6] Papadakis EP, Bernstein H. Elastic moduli of pyrolytic graphite. J Acoust Soc Am. 1963;35(4):521–4.

[7] Gebert JM, Reznik B, Piat R, Viering B, Weidenmann K, Wanner A, et al. Elastic constants of high-texture pyrolytic carbon measured by ultrasound phase spectroscopy. Carbon. 2010;48(12):3647 – 3650.

[8] Diss P, Lamon J, Carpentier L, Loubet JL, Kapsa P. Sharp indentation behavior of carbon/carbon composites and varieties of carbon. Carbon. 2002;40:2567–79.

[9] Guellali M, Oberacker R, Hoffmann MJ. Influence of heat treatment on microstructure and properties of highly textured pyrocarbons deposited during CVD at about 1100C and above 2000C. Composites Science and Technology. 2008;68(5):1122 – 30.

[10] Sauder C, Lamon J, Pailler R. The tensile properties of carbon matrices at temperatures up to 2200°C. Carbon. 2005;43(10):2054–65.

[11] Gross TS, Nguyen K, Buck M, Timoshchuk N, Tsukrov II, Reznik B, et al. Tension-compression anisotropy of in-plane elastic modulus for pyrolytic carbon. Carbon. 2011;49(6):2145 – 7.

[12] Gross TS, Timoshchuk N, Tsukrov II, Piat R, Reznik B. On the ability of nanoindentation to measure anisotropic elastic constants of pyrolytic carbon. Z Angew Math Mech. 2013;93(5):301–12.

[13] Penev ES, Artyukhov VI, Yakobson BI. Basic structural units in carbon fibers: Atomistic models and tensile behavior. Carbon. 2015;85:72 – 78.

[14] Kotakoski J, Meyer JC. Mechanical properties of polycrystalline graphene based on a realistic atomistic model. Phys Rev B. 2012;85:195447.

[15] Mortazavi B, Ahzi S. Thermal conductivity and tensile response of defective graphene: A molecular dynamics study. Carbon. 2013;63:460–470.

[16] Mortazavi B, Cuniberti G. Atomistic modeling of mechanical properties of polycrystalline graphene. Nanotechnology. 2014;25:215704.

[17] Farbos B, Weisbecker P, Fischer HE, Da Costa JP, Lalanne M, Chollon G, et al. Nanoscale structure and texture of highly anisotropic pyrocarbons revisited with transmission electron microscopy, image processing, neutron diffraction and atomistic modelling. Carbon. 2014;80:472–89.

[18] Leyssale JM, Da Costa JP, Germain C, Weisbecker P, Vignoles GL. An image guided atomistic reconstruction of pyrolytic carbons. App Phys Lett. 2009;95(23):231912.

[19] Leyssale JM, Da Costa JP, Germain C, Weisbecker P, Vignoles GL. Structural features of pyrocarbon atomistic models constructed from transmission electron microscopy images. Carbon. 2012;50(12):4388–400.

[20] Da Costa JP, Weisbecker P, Farbos B, Leyssale JM, Vignoles GL, Germain C. Investigating carbon materials nanostructure using image orientation statistics. Carbon. 2015;84:160–73.

[21] Weisbecker P, Leyssale JM, Fischer HE, Honkimäki V, Lalanne M, Vignoles GL. Microstructure of pyrocarbons from pair distribution function analysis using neutron diffraction. Carbon. 2012;50(4):1563–73.

[22] Freitas J. Unpublished preliminary results;.

[23] Brenner DW, Shenderova OA, Harrison JA, Stuart SJ, Ni B, Sinnott SB. A second-generation reactive empirical bond order (REBO) potential energy expression for hydrocarbons. J Phys: Condens Matter. 2002;14(4):783–802.

[24] Stuart SJ, Tutein AB, Harrison JA. A reactive potential for hydrocarbons with intermolecular interactions. J Chem Phys. 2000;112(14):6472–86.

[25] Lees AW, Edwards SF. The computer study of transport processes under extreme conditions. J Phys C. 1972;5:1921–9.

[26] Andersen HC. Molecular dynamics simulations at constant pressure and/or temperature. J Chem Phys. 1980;72:2384.

[27] Allen MP, Tildesley DJ. Computer Simulation of Liquids. Oxford University Press; 1987.

[28] Mehlig B, Heermann DW, Forrest BM. Hybrid Monte Carlo method for condensed-matter systems. Phys Rev B. 1992;45(2):679–685.

[29] Leyssale JM, Vignoles GL, Villesuzanne A. Rippled nanocarbons from periodic arrangements of reordered bivacancies in graphene or nanotubes. J Chem Phys. 2012;136:124705.

[30] Gamboa A, Vignoles GL, Leyssale JM. On the prediction of graphene's elastic properties with reactive empirical bond order potentials. Carbon. 2015;89:176–87.

[31] Blakslee OL, Proctor DG, Seldin EJ, Spence GB, Weng T. Elastic Constants of Compression-Annealed Pyrolytic Graphite. J Appl Phys. 1970;41:3373–3382.

[32] Bosak A, Krisch M. Elasticity of single-crystalline graphite: Inelastic X-ray scattering study. Phys Rev B. 2007;75:153408.

[33] Terrones H, Terrones M, Hernández E, Grobert N, Charlier JC, Ajayan PM. New Metallic Allotropes of Planar and Tubular Carbon. Phys Rev Lett. 2000;84(8):1716–1719.

[34] Marx DT, Riester L. Mechanical properties of carbon-carbon composite components determined using nanoindentation. Carbon. 1999;37(11):1679–1684.

[35] Hofmann G, Wiedenmeier M, Freund M, Beavan A, Hay J, Pharr GM. An investigation of the relationship between position within coater and pyrolytic carbon characteristics using nanoindentation. Carbon. 2000;38(5):645 – 653.